UC Irvine
UC Irvine Previously Published Works

Title
Limited–view radioacoustic imaging using parametric level sets

Permalink
https://escholarship.org/uc/item/2917q45g

Journal
Progress in Biomedical Optics and Imaging, 13931

ISSN
1605-7422

ISBN
978-1-5106-9799-7

Authors
Pandey, Prabodh Kumar
Gottam, Omprakash
Bjegovic, Kristina
et al.

Publication Date
2026

DOI
10.1117/12.3087299

Copyright Information
This work is made available under the terms of a Creative Commons Attribution License, available at https://creativecommons.org/licenses/by/4.0/

eScholarship.org Powered by the California Digital Library
University of California

Limited-view radioacoustic imaging using parametric level sets

Prabodh Kumar Pandey*[a], Omprakash Gottam[b], Kristina Bjegovic[c], Gilberto Gonzalez[d], Yong Chen[d] , Liangzhong Xiang**[a,c,e]

[a] Dept. of Radiological Sciences, University of California, Irvine, CA, 92697, USA; [b] Dept. of Electronics and Communications, Koneru Lakshmaiah Education Foundation, Hyderabad-500075, Telangana, India; [c] Dept. of Biomedical Engineering, University of California, Irvine, CA, 92697, USA; [d] Dept. of Radiation Oncology, University of Oklahoma Health Sciences Center, Oklahoma City, OK, 73104, USA; [e] Beckman Laser Institute, University of California, Irvine, CA, 92697, USA

ABSTRACT

Restricted transducer placement in clinical environments limits radiacoustic imaging (RAI) to incomplete angular measurements, producing characteristic artifacts—including spurious tails and missing features—that compromise dose reconstruction accuracy during radiation therapy monitoring. We address this limited-view challenge through two-stage reconstruction: parametric level-set optimization first identifies approximate dose region boundaries, then model-based inversion reconstructs detailed distributions within this spatially-constrained domain. Shape representation using radial basis functions reduces dimensionality from pixel-wise unknowns to geometric parameters describing piecewise-constant regions, while domain restriction concentrates measurement information onto fewer reconstruction variables. Validation studies encompass computational simulations and clinical LINAC experiments under limited as well as sparse angular coverage. In the simulated study, an elliptical source reconstructed from 120° detector aperture demonstrates improvements in ground-truth correlation from 0.86 (standard model-based) to 0.97 (shape-optimized). Experimental validation with clinical LINAC shows consistent gains: correlations versus full-view reconstructions increase from 0.87 to 0.90 for sparse four-detector arrays (144° coverage) and from 0.82 to 0.91 for seventeen-detector configurations (with 96° coverage). Shape-based spatial priors substantially reduce limited-view artifacts while improving quantitative accuracy and can be a crucial tool for solving the limited-view problem in RAI.

Keywords: Radiacoustic imaging, inverse problems, radiation dosimetry, shape reconstructions, level sets, ultrasound, imaging.

1. INTRODUCTION

Acoustic detection of radiation-induced ultrasound enables spatial mapping of deposited ionizing energy—a capability termed radiacoustic imaging (RAI) [1]. Research since its first demonstration in 2013 [2] has explored applications spanning structural visualization [3–12] and dose monitoring [13–23]. The fundamental principle of RAI is that short radiation pulses absorbed in tissue generate acoustic waves, which are detected by transducers. The signals thus obtained are then processed through reconstruction algorithms to map the energy distribution. Unlike CT [24], RAI's three-dimensional acoustic propagation enables volumetric imaging from a single radiation projection, simplifying experimental requirements. Radiation therapy (RT) conventionally relies on pre-treatment imaging [25–27] for dose delivery, which cannot account for anatomical or physiological changes occurring during therapy. No technique currently exists for real-time in vivo monitoring. RAI offers potential resolution of this gap and has progressed from laboratory demonstrations [2,14–16,20,22,28–30] to early-stage animal and patient studies [21,23]—garnering significant interest among radiation oncologists and physicists.

However, RAI faces a significant challenge: the limited-view problem. In many practical radiacoustic (RA) imaging setups, the number and placement of detectors are dictated by experimental and clinical constraints, which can lead to incomplete acoustic measurements. The reconstruction objective is to determine the initial pressure distribution (proportional to deposited dose) from these acquired signals. In comparison to the traditional approaches (back-projection [2,31] and time-reversal [32,33]), model-based (MB) algorithms [8–10] perform better in reducing artifacts. However, they haven't substantially resolved the limited-view issue that arises from the ill-posedness of the inverse problem [34–36].

*pkpandey@hs.uci.edu, **liangzhx@hs.uci.edu; https://truelab.medschool.uci.edu/

Medical Imaging 2026: Ultrasonic Imaging and Tomography, edited by Christian Boehm, Mohammad Mehrmohammadi, Shawn Liangzhong Xiang, Proc. of SPIE Vol. 13931, 1393105 · 2026 Published by SPIE
1605-7422 · doi: 10.1117/12.3087299

We employ a shape-based reconstruction approach that offers improved computational efficiency for ill-posed inverse problems. This method prioritizes identifying target boundaries over pixel-by-pixel recovery, significantly reducing the problem's dimensionality through level-set representations [37], which have demonstrated effectiveness across multiple imaging domains. Applications include: recovering abnormal absorption regions in diffusion optical tomography [37] using RBF-based parametric level-sets [38], detecting cancerous tissue through fluorescence optical tomography [39,40], characterizing regions with atypical pharmacokinetic behavior in fluorescence-acoustic imaging [41,42], identifying metallic objects from electromagnetic backscatter via shape optimization [43], and solving inverse obstacle scattering problems [44].

Our framework adapts the shape reconstruction methodology to reconstruct dose distribution shapes. The resulting shape serves as a spatial constraint for subsequent detailed reconstruction, confining the inverse problem to the identified region. This strategy mitigates limited-view artifacts and enhances reconstruction accuracy. In the rest of this paper, Section 2 formulates the RAI reconstruction problem, Section 3 details our numerical simulations and experimental validation studies, and Section 4 discusses the results. At the end, Section 5 concludes the work.

2. MATHEMATICAL FORMULATION

Radiacoustic imaging: Forward and inverse problem

Assuming instantaneous dose deposition, RA wave propagation follows:

$$\frac{\partial^2 p(\vec{r},t)}{\partial t^2} - v^2\nabla^2 p(\vec{r},t) = \Gamma H(\vec{r})\frac{\partial \delta(t)}{\partial t} \tag{1}$$

where $p(\vec{r},t)$ is propagating pressure, Γ is the Gruneisen parameter, v is the speed of sound, and H is the radiation energy distribution (RED). The solution to Eq. (1) is given by [35]:

$$p(\vec{r},t) = \frac{\Gamma}{4\pi v}\frac{\partial}{\partial t}\left(\frac{1}{vt}\int_{S(\vec{r},t)} H(\vec{r}')dS'(t)\right); \quad |\vec{r}-\vec{r}'| = vt\,, \tag{2}$$

where $S'(t)$ denotes a time-dependent spherical (circular for 2D) surface centered at a detector at $\vec{r}$ with radius vt. For this work, we will be focusing on 2D RAI. The discrete-domain representation of Eq.(2) is given as:

$$\underline{p} = \mathbf{M}\underline{h}\,. \tag{3}$$

Where $\underline{h}$ (size: $N \times 1$), and $\underline{p}$ (size: $(N_d.N_t) \times N$), are the discrete-domain representations of radiation energy deposition (RED) $H(\vec{r})$, measured pressure $p(\overrightarrow{r_d},t)$ $\mathbf{M}$ is the model-matrix (size: $(N_d.N_t) \times N$), with $\overrightarrow{r_d}$ being the co-ordinates of N_d transducer element and N_t is the number of time samples in each RA signal. For detailed derivation of Eq.(3) from Eq.(2), please refer to our previous work [8].

The inverse problem in RAI is to reconstruct the energy map ($\hat{\underline{h}}$) from the RA signals ($\underline{p}_{meas}$) and the MB image reconstruction algorithms aim to solve the corresponding regularized least-squares (LS) problem:

$$\hat{\underline{h}} = \arg\min_{\underline{h}} ||\underline{p}_{meas} - \mathbf{M}\underline{h}||_2^2 + \lambda^2||\mathbf{R}\underline{h}||_2^2\,, \tag{4}$$

where $||.||_2$ denotes the *L^2-norm.* $\mathbf{R}$ is the regularization matrix with λ being the regularization parameter.

Shape representation and reconstruction

For shape-based representation, we adopt a parametric level-set framework where the unknown h is modeled as piecewise constant, taking distinct values inside and outside the target region [40]

$$h(\Theta) = h^i\, H\big(\phi(r,\gamma)\big) + h^o\,(1 - H\big(\phi(r,\gamma)\big)) \tag{5}$$

Here $H(\phi)$ is the modified Heaviside function, h^i and h^o are the value of h inside and outside the target, and γ represents the shape defining parameters {α, β, χ_1, χ_2}, where α, β, and χ are the RBF coefficients, dilation factors, and center coordinates respectively for m radial basis functions (RBFs) used. The combined set of parameters is denoted by Θ = {h^i, h^o, α, β, χ_1, χ_2}. Following established approaches in optical tomography and fluorescence imaging, we use C^2 polynomial

RBFs of degree 5 as basis functions, which ensure compact support and sufficient smoothness [37,38]. The optimization problem then reduces to estimating the shape parameter set $\underline{\hat{\Theta}}$ that best fits the measured acoustic data, is given by:

$$\underline{\hat{\Theta}} = \arg\min_{\underline{h}} ||\underline{p}_{meas} - \mathbf{M}\underline{h}(\underline{\Theta})||_2^2 + \lambda^2||\underline{\Theta} - \underline{\Theta}_c||_2^2 \quad (6)$$

where $\underline{\Theta}_c$ is a priori known shape parameters, if available. This drastically reduces the number of unknowns from pixel-wise values to a small set of shape parameters including RBF weights, center locations, and dilation factors. We solve this nonlinear problem via trust-region regularized gradient optimization.

The reconstructed shape along with a small tolerance (~2-5 mm) is then considered as the shape-optimized region of interest (ROI) and the columns of model matrix **M** corresponding to the nodes outside this ROI are discarded. This new model-matrix is then employed to solve the MB LS problem (Eq.(4)) to obtain the shape-optimized MB (SOMB) reconstructions.

3. VALIDATION STUDIES

Computational study

To evaluate the efficacy of the proposed methodology, we performed a computational RAI study. An elliptical RED (with major and minor axes of 1.5cm and 0.75cm) was considered as the RA source, and the RA signals were simulated using the semi-analytic forward model [8,35] on a circular array (radius: 13 cm) consisting of 60 equispaced elements, as shown in Fig. 1(a). With respect to the center of the array, the elliptical source was centered at (+1cm, 0cm). The RA signals were simulated at 5 MHz sampling frequency using a grid resolution of 0.5 mm, using 10000 angular discretization for computing arc integrals.

The simulated RA measurements were then employed for model-matrix (MM) based MB RAI reconstructions in the ROI of 10 cm x 10 cm centered at the center of the transducer array. To avoid the inverse crime, the model-matrix was evaluated at 1mm grid resolution with 5000 angular discretization. This model-matrix was then employed for evaluating reconstructions using the proposed SOMB algorithm, and the result was compared with the traditional MB reconstructions. Steps for evaluating the proposed SOMB image reconstruction are shown in Fig. 1(b).

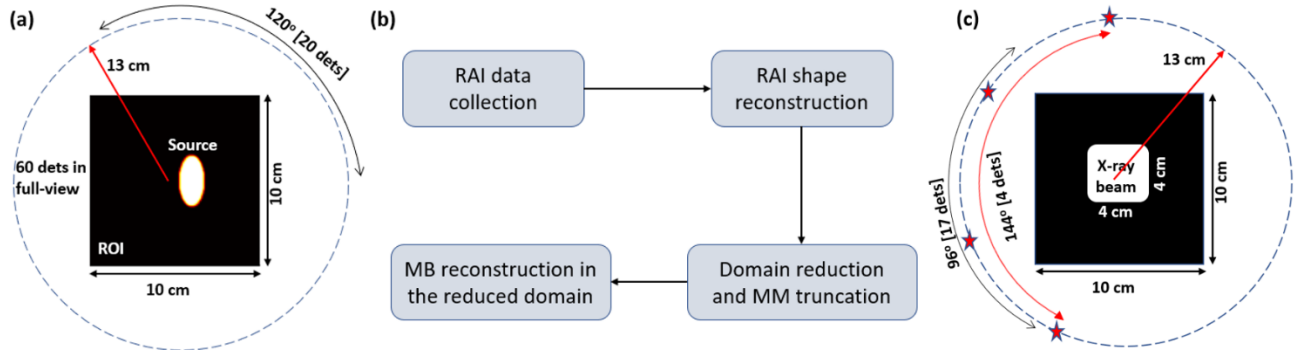

Figure 1. Methodology: (a) The setup for computational study, showing the RA source, detection geometry, and the ROI for reconstruction, (b) steps in evaluating shape-optimized model-based RAI reconstruction. (c) Settings for experimental studies.

Clinical experiment

Experiments employed a clinical Varian TrueBeam LINAC (10 MV) at OU Health Science Center, Oklahoma City, delivering radiation to a water-filled tank. Detection used an Olympus single-element probe (0.5 MHz center frequency, 100% bandwidth at -6 dB) positioned on a 130 mm circular trajectory centered on the beam axis, and waveforms were acquired at 60 equiangular positions spanning the full circle around the 4 × 4 cm² field. The RED was reconstructed in a 10 cm x 10cm domain concentric with the detection geometry. The full-view MB reconstruction obtained using all the 60 measurements was considered as the reference. The SOMB reconstructions were evaluated for two settings: (1) Four measurements spread over 144° and (2) 17 measurements spread over 96°, as shown in Fig. 1c.

4. RESULTS AND DISCUSSION

Results: Computational study

Fig. 2 shows the results from the simulated study. Standard model-based reconstruction (Fig. 2b) accurately identifies the elliptical source location compared to ground truth (Fig. 2a). However, characteristic limited-view artifacts appear as elongated tails extending from the source [36]. Moreover, the reconstructed values are also much lower in comparison to the ground truth. Shape optimization (Eq. 6) iteratively refines boundary estimates from an initial circular guess (3 cm radius), with convergence progression shown in Fig. 2e across 180 iterations. The evolution demonstrates convergence toward the source boundary. The final shape estimate with 2.5 mm buffer (Fig. 2c) constrains the second-stage (pointwise MB) reconstruction domain, producing Fig. 2d. The domain restriction eliminates most spurious artifacts and yields superior quantitative performance versus unconstrained MB. The improved fidelity manifests as correlation coefficient (CC) improvement from 0.86 (standard MB) to 0.97 (SOMB). Processing times using MATLAB's 'lsqr' were: 4 s (shape estimation), 0.02 s (full-domain MB), 0.008 s (restricted-domain MB).

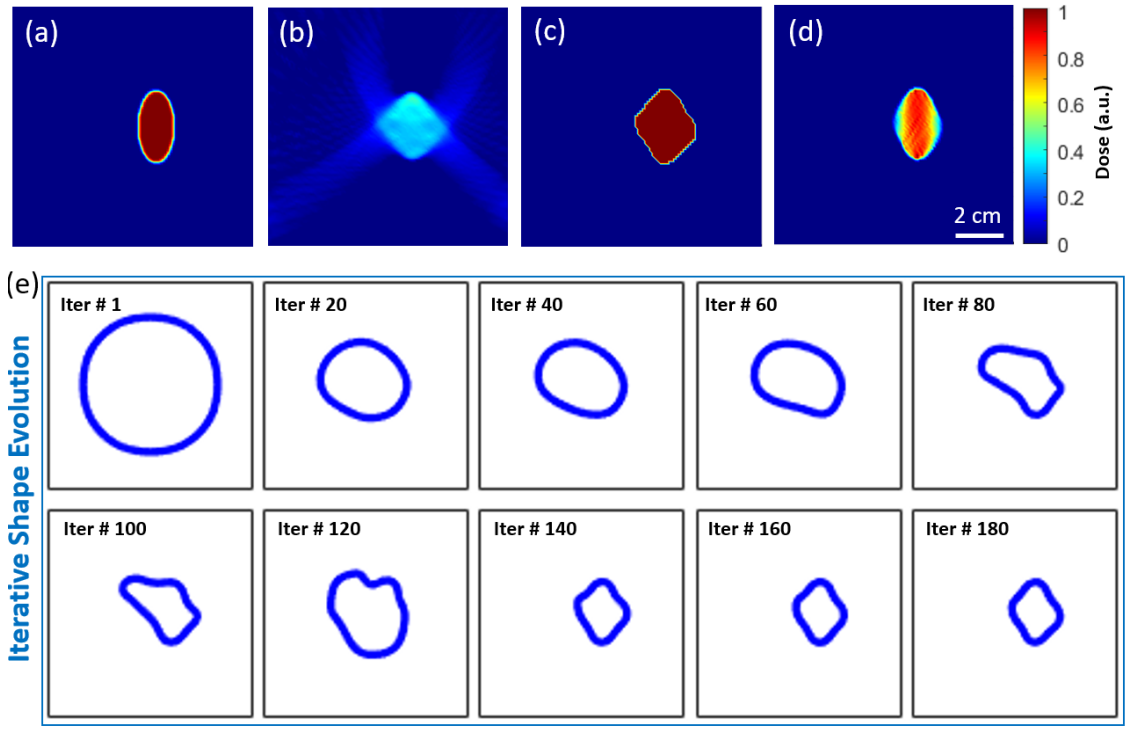

Figure 2. Computational study result: (a) The original RA source map, (b) standard MB reconstruction, (c) the shape reconstruction obtained from algorithm 1, and (d) the SOMB RAI reconstruction evaluation in the reduced region of interest. (e) The evolution of the reconstructed shape through solving Eq. (6) across iterations [ROI: 10 cm x 10 cm].

Results: Clinical experiment

Full-aperture reconstruction using all 60 angular measurements (Fig. 3a) served as the ground truth for LINAC X-ray-based validation study and yielded the expected 4 cm square beam geometry. Limited-aperture and sparse detection scenarios' standard MB and SOMB reconstructions were compared relative to this reference. For the ultra-sparse configuration (4 detectors, 144° coverage) test case, the standard MB inversion (Fig. 3b) produces distorted images with prominent limited-aperture and sparse detection artifacts. Level-set optimization accurately delineates the source (Fig. 3c). Restricting MB reconstruction to this region (Fig. 3d) yields cleaner images with correlation increasing from 0.87 to 0.90. Performance gains were more pronounced in the stronger limited-view scenario with 17/60 detectors (96° collection) as shown in Fig. 3e-g. Standard MB image (Fig. 3e) suffers from characteristic limited-aperture degradation—distortion and tail artifacts—achieving only CC = 0.82. SOMB reconstruction (Fig. 3g) markedly suppresses distortion and artifacts, improving correlation to 0.91.

The proposed two-stage framework leverages shape reconstruction to spatially constrain subsequent inversion. While boundary estimation incurs computational overhead (~4 seconds), this initial investment substantially reduces artifacts and enhances fidelity in the final reconstruction—benefits critically important for radiation therapy dosimetry. Translation to clinical practice requires addressing computational efficiency and dimensionality. GPU acceleration could reduce shape optimization time to enable near-real-time operation. In future work, we plan to extend this method to evaluate its efficacy for particle therapy radiation source and array-based detection, which is clinically more relevant.

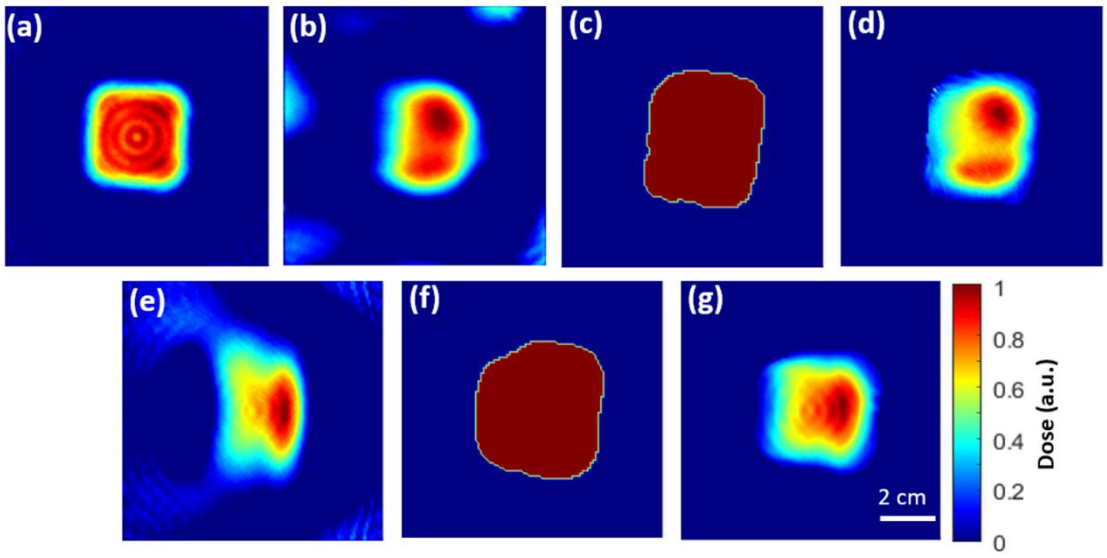

Figure 3. X-ray RAI experimental study result: (a) MB RAI reconstruction from full (60 detectors) data [used as ground truth], (b) standard MB reconstruction from 144^{o} angular coverage (with 4 detectors), (c) the shape reconstruction, and (d) the SOMB RAI reconstruction evaluated in the reduced ROI.(e) standard MB reconstruction from 96^{o} angular coverage (17 detectors), (f) the shape reconstruction, and (g) the SOMB RAI reconstruction evaluated in the reduced ROI.

5. CONCLUSION

Here, we proposed a shape-optimization based image reconstruction algorithm to overcome the challenges of the limited-view problem in the radiacoustic imaging, which aims to reconstruct the radiation dose from time-domain radiacoustic signals collected on the transducers placed around. The proposed method first solves an approximate homogeneous source using a shape reconstruction algorithm, which provides the approximate region of the deposited dose. Next, the model-based algorithm is employed for evaluating the reconstructions within this reduced domain. Across the in silico and experimental RAI studies, the reconstructions thus obtained were found to be of superior quality as compared to their typical model-based counterparts. While the current study demonstrates the capabilities of the proposed reconstruction framework on RAI measurements generated by an X-ray source and collected using single-element transducer scanning, we aim to extend this study for particle therapy sources and array-based detection to enhance clinical relevance and applicability.

ACKNOWLEDGEMENTS

This work was supported by the National Institutes of Health (R37CA240806, U01CA288351, R50CA283816). The authors would like to acknowledge the support from UCI Chao Family Comprehensive Cancer Center (No. P30CA062203).

REFERENCES

[1] Y. Xu and S. L. Xiang, Radiacoustic imaging, Nat Rev Phys (2025).

[2] L. Xiang, B. Han, C. Carpenter, G. Pratx, Y. Kuang, and L. Xing, X-ray acoustic computed tomography with pulsed x-ray beam from a medical linear accelerator, Medical Physics **40**, 010701 (2013).
[3] L. Xiang, S. Tang, M. Ahmad, and L. Xing, High Resolution X-ray-Induced Acoustic Tomography, Sci Rep **6**, 26118 (2016).
[4] S. Tang, K. Yang, Y. Chen, and L. Xiang, X-ray-induced acoustic computed tomography for 3D breast imaging: A simulation study, Medical Physics **45**, 1662 (2018).
[5] D. Lee, E.-Y. Park, S. Choi, H. Kim, J. Min, C. Lee, and C. Kim, GPU-accelerated 3D volumetric X-ray-induced acoustic computed tomography, Biomed. Opt. Express **11**, 752 (2020).
[6] Y. Li, P. Samant, S. Wang, A. Behrooz, D. Li, and L. Xiang, 3-D X-Ray-Induced Acoustic Computed Tomography With a Spherical Array: A Simulation Study on Bone Imaging, IEEE Trans. Ultrason., Ferroelect., Freq. Contr. **67**, 1613 (2020).
[7] E. Robertson, P. Samant, S. Wang, T. Tran, X. Ji, and L. Xiang, X-Ray-Induced Acoustic Computed Tomography (XACT): Initial Experiment on Bone Sample, IEEE Trans. Ultrason., Ferroelect., Freq. Contr. **68**, 1073 (2021).
[8] P. K. Pandey, S. Wang, H. O. Aggrawal, K. Bjegovic, S. Boucher, and L. Xiang, Model-Based X-Ray-Induced Acoustic Computed Tomography, IEEE Trans. Ultrason., Ferroelect., Freq. Contr. **68**, 3560 (2021).
[9] P. K. Pandey, S. Wang, and L. Xiang, *Model Based Reconstruction Algorithm for X-Ray Induced Acoustic Tomography*, in *Medical Imaging 2021: Physics of Medical Imaging*, edited by H. Bosmans, W. Zhao, and L. Yu (SPIE, Online Only, United States, 2021), p. 128.
[10] P. K. Pandey, S. Wang, L. Sun, L. Xing, and L. Xiang, Model-Based 3-D X-Ray Induced Acoustic Computerized Tomography, IEEE Trans. Radiat. Plasma Med. Sci. **7**, 532 (2023).
[11] P. K. Pandey, G. Gonzalez, K. Bjegovic, L. Sun, Y. Chen, and L. Xiang, 3D protoacoustic radiography: A proof of principle study, Applied Physics Letters **126**, 074102 (2025).
[12] S. Wang, P. K. Pandey, G. Lee, R. J. P. Van Bergen, L. Sun, Y. Xu, and L. Xiang, X-ray–induced acoustic computed tomography: 3D X-ray absorption imaging from a single view, Sci. Adv. **10**, eads1584 (2024).
[13] S. Hickling, M. Hobson, and I. El Naqa, Feasibility of X-Ray Acoustic Computed Tomography as a Tool for Noninvasive Volumetric In Vivo Dosimetry, International Journal of Radiation Oncology*Biology*Physics **90**, S843 (2014).
[14] S. Hickling, H. Lei, M. Hobson, P. Léger, X. Wang, and I. El Naqa, Experimental evaluation of x-ray acoustic computed tomography for radiotherapy dosimetry applications, Medical Physics **44**, 608 (2017).
[15] S. Hickling, M. Hobson, and I. El Naqa, Characterization of X-Ray Acoustic Computed Tomography for Applications in Radiotherapy Dosimetry, IEEE Trans. Radiat. Plasma Med. Sci. **2**, 337 (2018).
[16] J. Kim, E.-Y. Park, Y. Jung, B. C. Kim, J. H. Kim, C.-Y. Yi, I. J. Kim, and C. Kim, X-Ray Acoustic-Based Dosimetry Using a Focused Ultrasound Transducer and a Medical Linear Accelerator, IEEE Trans. Radiat. Plasma Med. Sci. **1**, 534 (2017).
[17] H. Lei, W. Zhang, I. Oraiqat, Z. Liu, J. Ni, X. Wang, and I. El Naqa, Toward *in vivo* dosimetry in external beam radiotherapy using x-ray acoustic computed tomography: A soft-tissue phantom study validation, Medical Physics **45**, 4191 (2018).
[18] *Water Dosimetry Device Using X-Ray Induced Ultrasonic Waves*, (n.d.).
[19] I. Oraiqat, W. Zhang, D. Litzenberg, K. Lam, N. Ba Sunbul, J. Moran, K. Cuneo, P. Carson, X. Wang, and I. El Naqa, An ionizing radiation acoustic imaging (iRAI) technique for real-time dosimetric measurements for FLASH radiotherapy, Medical Physics **47**, 5090 (2020).
[20] S. Wang, G. Gonzalez, L. Sun, Y. Xu, P. Pandey, Y. Chen, and S. Xiang, Real-time tracking of the Bragg peak during proton therapy via 3D protoacoustic Imaging in a clinical scenario, Npj Imaging **2**, 34 (2024).
[21] W. Zhang et al., Real-time, volumetric imaging of radiation dose delivery deep into the liver during cancer treatment, Nat Biotechnol **41**, 1160 (2023).
[22] L. Sun, G. Gonzalez, P. K. Pandey, S. Wang, K. Kim, C. Limoli, Y. Chen, and L. Xiang, Towards quantitative in vivo dosimetry using x-ray acoustic computed tomography, Medical Physics **50**, 6894 (2023).
[23] K. Bjegovic et al., 4D in vivo dosimetry for a FLASH electron beam using radiation-induced acoustic imaging, Phys. Med. Biol. **69**, 115053 (2024).
[24] G. T. Herman, *Fundamentals of Computerized Tomography* (Springer London, London, 2009).
[25] U. Schneider, E. Pedroni, and A. Lomax, The calibration of CT Hounsfield units for radiotherapy treatment planning, Phys. Med. Biol. **41**, 111 (1996).
[26] G. C. Pereira, M. Traughber, and R. F. Muzic, The Role of Imaging in Radiation Therapy Planning: Past, Present, and Future, BioMed Research International **2014**, 1 (2014).

[27] S. J. Gardner, J. Kim, and I. J. Chetty, Modern Radiation Therapy Planning and Delivery, Hematology/Oncology Clinics of North America **33**, 947 (2019).
[28] G. Gonzalez, K. Prather, P. K. Pandey, L. Sun, J. Caron, S. Wang, S. Ahmad, L. Xiang, and Y. Chen, Single-Pulse X-ray Acoustic Computed Tomographic Imaging for Precision Radiation Therapy, Advances in Radiation Oncology **8**, 101239 (2023).
[29] W. Assmann et al., Ionoacoustic characterization of the proton Bragg peak with submillimeter accuracy, Medical Physics **42**, 567 (2015).
[30] J. Schauer et al., Proton beam range verification by means of ionoacoustic measurements at clinically relevant doses using a correlation-based evaluation, Front. Oncol. **12**, 925542 (2022).
[31] M. Xu and L. V. Wang, Universal back-projection algorithm for photoacoustic computed tomography, Phys. Rev. E **71**, 016706 (2005).
[32] F. Forghani, A. Mahl, T. J. Patton, B. L. Jones, M. A. Borden, D. C. Westerly, C. Altunbas, M. Miften, and D. H. Thomas, Simulation of x-ray-induced acoustic imaging for absolute dosimetry: Accuracy of image reconstruction methods, Medical Physics **47**, 1280 (2020).
[33] B. E. Treeby and B. T. Cox, k-Wave: MATLAB toolbox for the simulation and reconstruction of photoacoustic wave fields, J. Biomed. Opt. **15**, 021314 (2010).
[34] Y. Han, V. Ntziachristos, and A. Rosenthal, Optoacoustic image reconstruction and system analysis for finite-aperture detectors under the wavelet-packet framework, J. Biomed. Opt **21**, 016002 (2016).
[35] A. Buehler, A. Rosenthal, T. Jetzfellner, A. Dima, D. Razansky, and V. Ntziachristos, Model-based optoacoustic inversions with incomplete projection data, Medical Physics **38**, 1694 (2011).
[36] kun wang, Three-Dimensional Photoacoustic Computed Tomography: Imaging Models and Reconstruction Algorithms., Washington University in St. Louis, 2012.
[37] A. Aghasi, M. Kilmer, and E. L. Miller, Parametric Level Set Methods for Inverse Problems, SIAM J. Imaging Sci. **4**, 618 (2011).
[38] H. Wendland, *Scattered Data Approximation*, 1st ed. (Cambridge University Press, 2004).
[39] O. Gottam, N. Naik, and S. Gambhir, *Shape Based Pharmacokinetic Fluorescence Optical Tomography*, in *Biomedical Imaging and Sensing Conference*, edited by O. Matoba, Y. Awatsuji, T. Yatagai, and Y. Aizu (SPIE, Yokohama, Japan, 2018), p. 18.
[40] O. Gottam and N. Naik, Parameterized level-set based pharmacokinetic fluorescence optical tomography using the regularized Gauss–Newton filter, J. Biomed. Opt. **24**, 1 (2018).
[41] O. Gottam, N. Naik, P. K. Pandey, and S. Gambhir, *RBF Level-Set Based Fluorescence Photoacoustic Pharmacokinetic Tomography*, in *Imaging and Applied Optics Congress* (Optica Publishing Group, Washington, DC, 2020), p. JF4E.7.
[42] O. Gottam, N. Naik, P. Kumar Pandey, and S. Gambhir, RBF level-set based fully-nonlinear fluorescence photoacoustic pharmacokinetic tomography, Inverse Problems in Science and Engineering **29**, 3227 (2021).
[43] T. Bonnafont and F. Caubet, *A Robust Inverse Scattering Method Based on Shape Optimization*, in *2023 IEEE Conference on Antenna Measurements and Applications (CAMA)* (IEEE, Genoa, Italy, 2023), pp. 1–6.
[44] L. Audibert, H. Haddar, and X. Liu, An Accelerated Level-Set Method for Inverse Scattering Problems, SIAM J. Imaging Sci. **15**, 1576 (2022).
[45] L. Ding, D. Razansky, and X. L. Dean-Ben, Model-Based Reconstruction of Large Three-Dimensional Optoacoustic Datasets, IEEE Trans. Med. Imaging **39**, 2931 (2020).